Research Article

Muchammad Tamyiz*, Ruey-an Doong

Synergetic effect of adsorption and photocatalysis by zinc ferrite-anchored graphitic carbon nitride nanosheet for the removal of ciprofloxacin under visible light irradiation

https://doi.org/10.1515/chem-2022-0304 received January 31, 2023; accepted March 1, 2023

Abstract: Ciprofloxacin (CIP) belongs to the fluoroquinolone antibiotic family. It is mostly used for the treatment of bacterial infections and highly recalcitrant to naturally decompose. The nanocomposite was successfully constructed by zinc ferrite nanoparticle anchored onto graphitic carbon nitride nanosheet (ZFNP-CNNS). The structural, morphological, and optical properties of the ZFNP-CNNS nanocomposite were investigated. Moreover, the enhanced photocatalytic performance of the ZFNP-CNNS nanocomposite was a result of the synergetic effect between adsorption and photocatalysis. The adsorption study showed that the ZFNP-CNNS nanocomposite has heterogeneous active sites with multilayers and the maximum CIP adsorption capacity was 15.49 mg g^{-1} . However, the photodegradation efficacy of CIP reached up to five times compared to that of pristine CNNS. The high adsorption-photocatalytic synergetic effect of the ZFNP-CNNS nanocomposite has great application in wastewater treatment.

Keywords: antibiotic, ciprofloxacin, photodegradation, ZFNP-CNNS nanocomposite

1 Introduction

The necessity for medicine and pharmaceutical products, especially antibiotics, is unavoidable. However, antibiotics contribute to the increasing amount of pollutants, which are damaging the environment. Moreover, antibiotics are known as compounds that are difficult to degrade by traditional wastewater treatments, including filtration, coagulation, and sedimentation [1,2]. Photocatalysis is one of the auspicious technologies that is of low cost, highly efficient in the degradation of pollutants, eco-friendly and nontoxic, and secondary pollution free [3-5]. Photocatalysis can effectively degrade antibiotics, such as ciprofloxacin (CIP), enrofloxacin, and sulfamethazine, from aqueous environments [6–8]. The graphitic-like carbon nitride (g-C₃N₄, CN) has been approved as a potential photocatalyst material, which is suitable for some applications, such as carbon dioxide reduction, water splitting, and degradation of emerging pollutants [9]. Moreover, CN has interesting properties because of the appropriate bandgap (2.7 eV), physical and chemical stabilities, nontoxicity, low cost, and easy and scalable mass production [10].

Two-dimensional morphology of CN (carbon nitride nanosheet [CNNS]) has several advantages because it possesses high specific surface area and thinner layer compared to other CN morphologies, such as 0D, 1D, and 3D [11]. A considerable specific surface of CNNS provides more active sites and also enhances the separation rate of photogenerated electrons and holes (e^-h^+). However, the CNNS has several drawbacks which are affecting its photocatalytic performance, such as insufficient utilization of visible light and low transfer of photogenerated e^-h^+ pairs which participate in the reduction and oxidation reactions [11]. Therefore, the heterojunction formation with other photocatalyst materials can address these disadvantages and also enhance photocatalytic performance. The metal oxide shows a preferably visible light

^{*} Corresponding author: Muchammad Tamyiz, Institute of Analytical and Environmental Sciences, National Tsing Hua University, 101, Section 2, Kuang Fu Road, Hsinchu, 300044, Taiwan; Department of Biomedical Engineering and Environmental Sciences, National Tsing Hua University, Hsinchu, 300044, Taiwan; Department of Environmental Engineering, Universitas Nahdlatul Ulama Sidoarjo, Sidoarjo, 61234, Indonesia, e-mail: m_tamyiz.tkl@unusida.ac.id Ruey-an Doong: Institute of Analytical and Environmental Sciences, National Tsing Hua University, 101, Section 2, Kuang Fu Road, Hsinchu, 300044, Taiwan

response, especially bimetallic oxides with superior photocatalytic performance than single transition metal oxides [12]. Spinel ferrite is an attractive bimetallic oxide due to its physicochemical stability, dynamic magnetic and interesting optical properties. Zinc ferrite nanoparticles (ZnFe₂O₄, ZFNP) became hot attraction materials because of their sustainable synthesis, simplicity of preparation, wellcontrolled stoichiometry, suitable particle size, rapid time processing, narrow bandgap (~1.9 eV), acceptable synthesis temperatures, and scalable mass production [13,14]. On the other hand, the insufficient effectiveness of ZFNP brings out a terrible photocatalytic performance and a speedy electron-hole recombination process [15]. As a result, some endeavors have been made to address these issues, such as heterojunction formation using different materials.

In this study, the zinc ferrite nanoparticle anchored onto graphitic carbon nitride nanosheet (ZFNP-CNNS) nanocomposite was successfully synthesized with the adsorption-photocatalysis synergetic effect for the photodegradation of CIP. The drawback of CNNS due to broad bandgap energy (2.83 eV) could be addressed by the participation of ZFNP in the ZFNP-CNNS nanocomposite. This work has been dedicated to acquiring narrowly the bandgap of the ZFNP-CNNS nanocomposite of 2.66 eV. Consequently, the ZFNP-CNNS nanocomposite could extend the absorption of light and increase the photodegradation performance of CIP. The ZFNP-CNNS nanocomposite was appropriate to the specification of an ideal photocatalyst as it (i) harvests sunlight with a broad wavelength, (ii) has a high surface area, and acts as a mesoporous photocatalyst, (iii) has eminent reusability, (iv) has effortless separation, and (v) has a durability of photocorrosion.

2 Materials and methods

2.1 Materials

Each chemical used in the synthesis of the ZFNP–CNNS nanocomposite was of analytical grade and used without any further treatment, including urea (99%), dicyandiamide (99%), zinc nitrate hexahydrate (99%), iron(III) nitrate-9-hydrate (98%), 1-pentanol (\geq 98%), oleic acid (90%), oleylamine (70%), ethanol (\geq 99%), and CIP (98%). All solutions were prepared using ultrapure water (18.2 M Ω cm).

2.2 Synthesis of the ZFNP-CNNS nanocomposite

The bulk CN was prepared by a combination of urea and dicyandiamide (2:1 w/w) and calcinated at 550°C, 2°C min⁻¹, for 4 h in air. The CNNS was synthesized by thermal exfoliation at 520°C, 5°C min⁻¹, for 2 h in atmospheric air condition. In the meantime, the ZFNP was synthesized by the hydrothermal method. An amount of deionized water was used to dissolve iron nitrate and zinc nitrate in a molar ratio of 2:1 under vigorous stirring. Then, 60 mL of pentanol as an organic solvent was added to the solution, followed by oleic acid and oleylamine in a molar ratio of 1:1. The NaOH solution was added until the pH value attained 11 and then the solution was stirred continuously for 1h. The mixture was transferred to a Teflon tube and subjected to the hydrothermal process at 180°C for 16 h. Furthermore, the ethanol/n-hexane (1/3, v/v) mixture was used as a washing solution to remove impurities in the ZFNP. The ZFNP-CNNS nanocomposites were synthesized by mixing a certain mass of CNNS with loadings of ZFNPs in 15 mL of ethanol. The mixture was filtered and dried for 6 h at 60°C. Then, the mixture was calcinated at 400°C, 5°C min⁻¹, for 2 h.

2.3 Characterization of the ZFNP-CNNS nanocomposite

The X-ray diffraction (XRD) patterns were determined using Bruker D8 Advance. The surface morphological characteristics were determined using SEM (JEOL, JSM-6490LV) equipped with an EDX spectrometer (JEOL, Centurio) and TEM (Hitachi S-3000N). The absorption spectra were recorded in a 350–800 nm range using Hitachi U-4100 UV-vis spectrophotometer. A Nicolet 6700 spectrophotometer was used to obtain the functional group information of the materials. The specific surface area was measured using Micromeritics ASAP 2020.

2.4 Photocatalytic degradation experiments

The adsorption activity was determined in the as-prepared sample that was treated in the dark condition with a solution of 20 mL of CIP ($10 \, \text{mg L}^{-1}$) at a neutral pH and a temperature of 25 \pm 2°C. To study the adsorption behavior, 0.5 g L⁻¹ of CNNS, ZFNP, and ZFNP–CNNS was added to the CIP solution. The photocatalytic activity

of nanocomposites was determined in the as-prepared sample when exposed to eight visible light sources (each 8 W). The concentration of residual CIP and the adsorption capacity were determined by high-performance liquid chromatography (HPLC; Agilent 1200).

2.5 Adsorption kinetics and isotherms model

The adsorption kinetics can be expressed by the reaction order, adsorption capacity, and adsorption rate. Lagergren kinetic models for the pseudo-first-order (PFO) and pseudo-second-order (PSO) were used to determine the CIP adsorption on the surface of the ZFNP–CNNS. The linear forms of PFO (equation (1)) and PSO (equation (2)) have been introduced to determine the adsorption process characteristic.

$$\ln(q_{\rm e}-q_t)=\ln q_{\rm e}-K_1t,\tag{1}$$

$$\frac{t}{q_t} = \frac{1}{K_2 + q_e^2} + \frac{1}{q_e}t,\tag{2}$$

where q_t and q_e are the capacity of CIP adsorption on the photocatalytic adsorbent at a particular time and the quantity of CIP adsorption at an equilibrium time (mg g⁻¹), respectively. Furthermore, K_1 and K_2 are the coefficient of PFO (min⁻¹) and that of PSO (mg g⁻¹ min⁻¹), respectively. Meanwhile, the adsorption isotherm mechanism can provide information about the distribution of homogeneous or heterogeneous CIP molecules at the liquid and solid interface in equilibrium time, active sites, monolayer or multilayer formation, and adsorption characteristics [16–18]. Furthermore, the nonlinear Sips (equation (3)) and Temkin (equation (4)) isotherms were applied to understand the isotherm mechanism of the photocatalytic adsorbent [19].

$$q_{\rm e} = \frac{K_{\rm a}(C_{\rm e})^n}{1 + K_{\rm a}(C_{\rm e})^n} q_{\rm m},$$
 (3)

$$q_{\rm e} = \frac{RT}{B_{\rm T}} \ln K_T C_{\rm e},\tag{4}$$

where K_a and n are the capacity and intensity of adsorption (L mg⁻¹), respectively. Moreover, R is the ideal gas constant (8.314 J mol⁻¹ K⁻¹), T is an absolute temperature (K), B_T is the Temkin isotherm constant (J mol⁻¹), and K_T is the Temkin isotherm binding constant (L g⁻¹).

3 Results and discussion

3.1 Structure and optical characterization of the ZFNP-CNNS nanocomposite

The XRD patterns of CNNS, ZFNP, and ZFNP-CNNS nanocomposites are shown in Figure 1a. The XRD-specific peak profiles of pure CNNS and ZFNP are found at 2θ = 27.6 and 35.4°, corresponding to the crystallographic planes (002) and (311), respectively [20,21]. However, the XRD patterns of pristine CNNS and ZFNP coincide with the JCPDS card Nos 87-1526 and 89-1010, respectively. No other impurity phases are obtained, thus representing the highly crystalline nature obtained from the pure CNNS and ZFNP. The XRD patterns of the ZFNP-CNNS nanocomposite reveal a series of diffraction peaks located at 12.8, 27.6, 29.7, 35.4, 42.3, 53.4, 56.8, and 62.3°, corresponding to the crystallographic planes (100), (002), (220), (311), (4 0 0), (4 2 2), (5 1 1), and (4 4 0) [13,22-24]. On the other hand, the suppression of the (002) peak for CNNS is presumably attributable to embedding ZFNP nanoparticles on the ZFNP-CNNS surface. The Scherrer equation is used to determine the crystallite sizes for CNNS, ZFNP, and ZFNP-CNNS nanocomposites, namely, 8.2, 23.2, and 18.5 nm, respectively. Meanwhile, the percentages of crystallinity of CNNS, ZFNP, and ZFNP-CNNS nanocomposites are 38, 83, and 50%, respectively. Furthermore, the crystallinity of the ZFNP-CNNS nanocomposite is higher than that of pure CNNS due to the introduction of ZFNPs on the ZFNP-CNNS surface.

Figure 1b shows the fourier transform infrared spectroscopy (FT-IR) transmission spectra of pristine CNNS, ZFNP, and ZFNP-CNNS nanocomposites. For CNNS, the stretching vibrational nodes of the repeating units deprived of heptazine (C-N heterocycles) are observed in 1,150-1,700 cm⁻¹. The out-of-plane breathing modes of heptazine rings correspond to the sharp peaks at 812 cm⁻¹. The stretching vibrations of N-H groups are observed in 3,000-3,500 cm⁻¹. The ZFNPs, either inverse or standard spinel oxide, have two evident infrared active modes at 563 and 432 cm⁻¹, corresponding to the characteristic peaks of octahedral and tetrahedral sites for Fe-O and Zn-O of the ZFNP, respectively [25,26]. Furthermore, the absorption bands at 1,635 and 3,420 cm⁻¹ are defined as the surface hydroxyl bending and the H₂O stretching vibration that were adsorbed on the surface of ZFNP [27]. The sharp band at 1,384 cm⁻¹ is associated with a nitrate group due to metal nitrate salts as precursors in synthesizing ZFO nanoparticles [26]. Also,

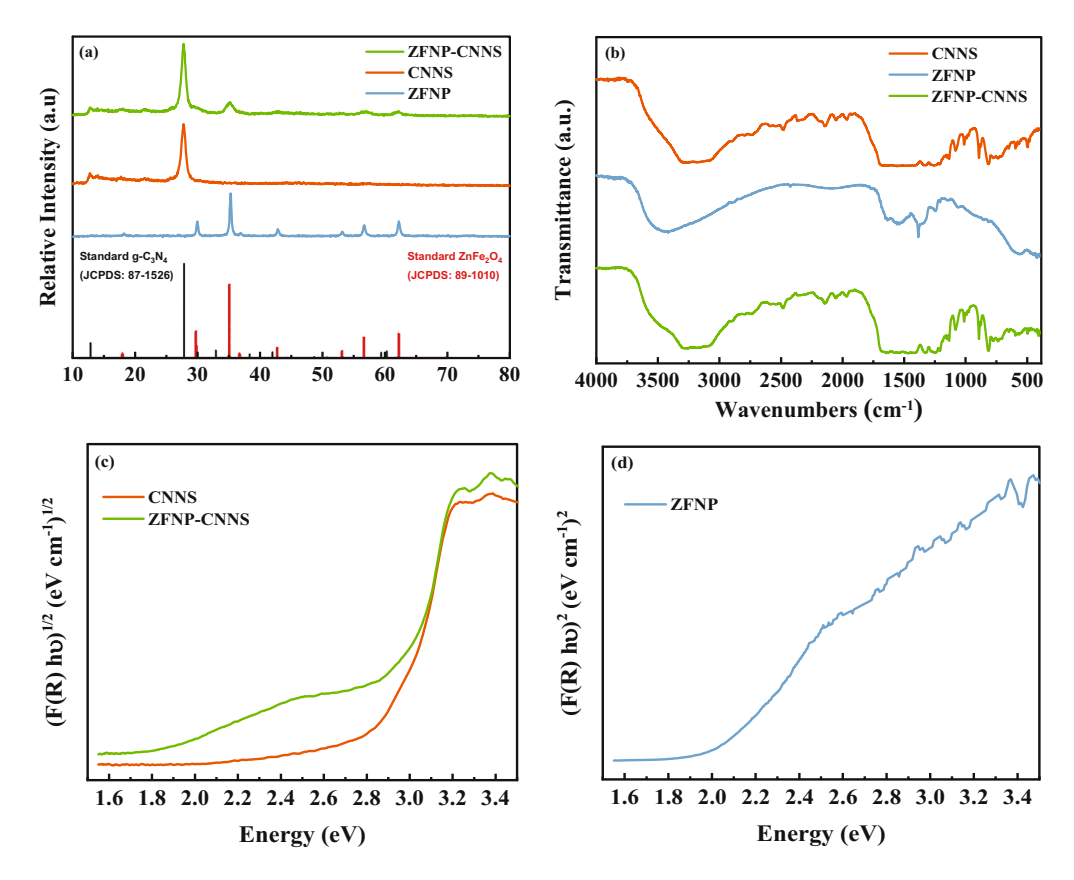


Figure 1: (a) XRD patterns, (b) FT-IR spectra, and (c and d) Kubelka-Munk extrapolation of CNNS, ZFNP, and ZFNP-CNNS nanocomposite.

the marked peaks at 812, 1,246, 1,416, and 1,557 cm⁻¹ indicate a slightly strong absorption on ZFNP–CNNS samples, signifying that the CNNS covalent bond has a change in its coordination environment.

The reflectance spectra of diffuse reflectance spectroscopy were applied to determine the optical bandgap of the as-prepared samples. Based on the Kubelka–Munk function, the bandgap is found at 2.83, 1.82, and 2.66 eV for CNNS, ZFNP, and ZFNP–CNNS nanocomposites, respectively. The CNNS and ZFNP–CNNS have an absorption coefficient with an indirect bandgap. In contrast, ZFNP has a direct semiconductor bandgap, as shown in Figure 1c and d [28,29]. Compared to pristine CNNS, the ZFNP–CNNS nanocomposite could absorb broader visible light and possibly increase the generation of e^-h^+ pairs.

The morphological characteristics, composition of elements, particle shapes, and size distribution of the as-prepared samples were examined by SEM, TEM, and EDX, respectively. Figure 2a represents the SEM images of CNNS-like sheets, and the ZFNP is nanospherical in shape with an average size of 24 nm, as shown in Figure 2b. The crystallite sizes of ZFNP (23.2 nm) calculated by the XRD data are appropriate. The anchored ZFNPs on the CNNS surface are ubiquitously distributed,

as depicted in Figure 2c. The EDX spectra in Figure 2d reveal that ZFNP anchored successfully to the CNNS surface, as can be verified from the elemental weight percentage of ZFNP–CNNS. Furthermore, the abovementioned observations justify the formation of the ZFNP–CNNS heterojunction.

3.2 CIP degradation via synergistic adsorption-photocatalysis

The dark and light modes were used to assess the synergistic effect of adsorption and photocatalytic degradation against CIP with the ZFNP–CNNS nanocomposite. The adsorption experiment of CIP solution 10 mg L $^{-1}$ (20 mL, pH 7) was controlled in the dark mode to fully eliminate the photocatalytic effect. Moreover, the contact time to achieve equilibrium and adsorption saturation was 30 min. The brisk adsorption of the as-prepared sample was noticed in the first 10 min, continued by slower adsorption, and proceeded until saturation was reached, as depicted in Figure 3a. The ZFNP–CNNS nanocomposite and CNNS had a maximum adsorption capacity of 9.04 and 5.70 mg g $^{-1}$, respectively. It corresponded to the CIP removal of 44 and

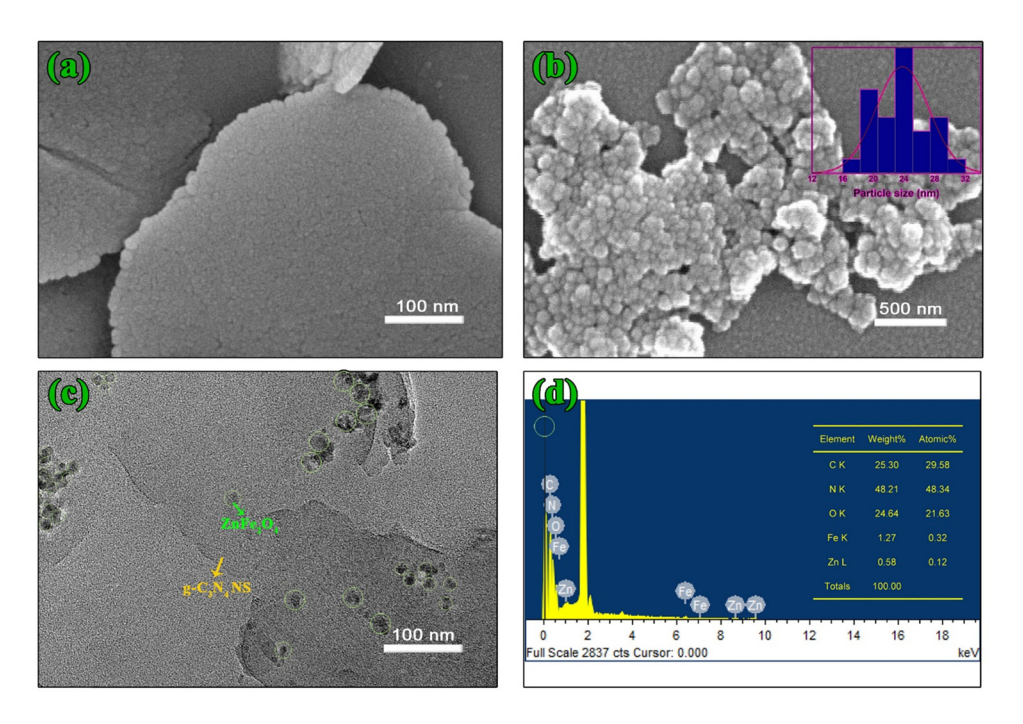


Figure 2: SEM images of (a) CNNS, (b) ZFNP, (c) TEM image of ZFNP-CNNS, and (d) EDX spectra of ZFNP-CNNS.

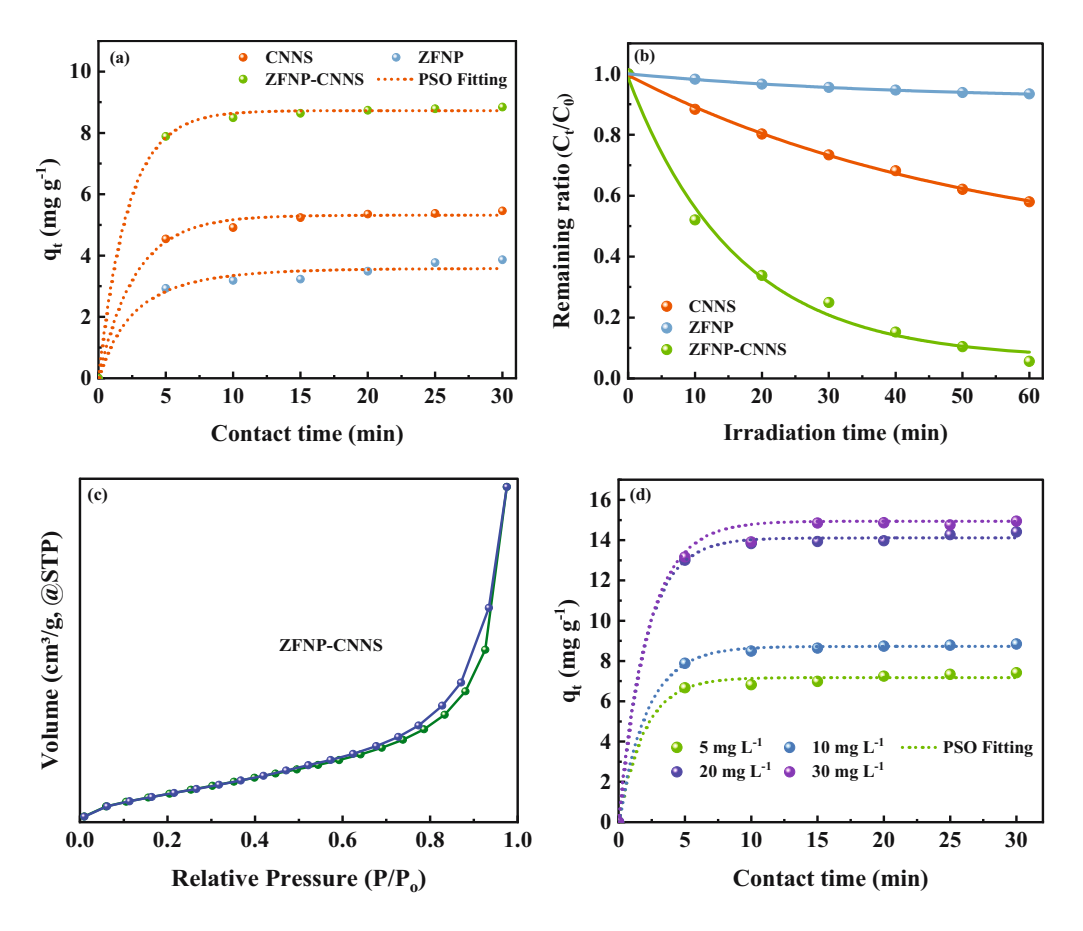


Figure 3: (a) The adsorption kinetic and PSO exponential fitting, (b) the photocatalytic activity of CNNS, ZFNP, and ZFNP-CNNS nano-composites, (c and d) N_2 adsorption-desorption curve and the concentration-dependent adsorption kinetic of the ZFNP-CNNS nanocomposite.

27% by the adsorption process. Meanwhile, the CIP removal rate using ZFNP was 18%, and the maximum adsorption capacity was 4.18 mg g^{-1} .

The narrow bandgap energy (1.82 eV) of the ZFNP caused by e⁻-h⁺ recombination potential is more significant. Consequently, the photocatalytic performance of ZFNP was lowest (24%) within 60 min compared with the other two synthesized photocatalyst materials, as depicted in Figure 3b. Moreover, the CNNS and ZFNP-CNNS represent a higher CIP photodegradation than the ZFNP, i.e., 58 and 97%, respectively. The fact is that the bandgap energy of the ZFNP-CNNS (2.66 eV) is lower than that of pure CNNS (2.83 eV), which allows more capturing of visible light and reduces the e⁻-h⁺ recombination rate. The experimental data revealed that photocatalytic degradation followed the linear fitting of PFO kinetic. Then, synergistically, CIP removal between adsorption and photocatalysis is consistently shown by the ZFNP-CNNS nanocomposites that showed the best performance. In the ZFNP-CNNS nanocomposite, the CIP molecules could be adsorbed and effectively enriched by the lamellar CNNS, which provides a high surface area and has the most mesoporous sites. Thus, it could quickly reduce the CIP concentration in the solution and increase the probability of CIP contact with the ZFNP-CNNS nanocomposite and further photodegradation by the reactive oxygen species [30]. This result

attests to the heterojunction formation system between ZFNP and CNNS and increases the photocatalytic activity.

Hereafter, the PSO kinetic has a better fitting concurrence than the PFO fitting, with the theoretical value of $q_{\rm e}$ being near to q_e of the experiment. The K_d value of the ZFNP-CNNS nanocomposite (0.904 L g⁻¹) has higher adsorption and photocatalytic performance compared to that of ZFNP and CNNS, namely, 0.418 and 0.570 L g⁻¹, respectively. On other hand, Figure 3c exhibits the Brunauer-Emmett-Teller (BET) analysis of the ZFNP-CNNS nanocomposite, which shows a type-IV isotherm with H3 hysteresis and has a specific surface area of $134\,\mathrm{m}^2\,\mathrm{g}^{-1}$. This result implies that the high K_d value of the ZFNP-CNNS nanocomposite is in line with the high surface area of the ZFNP-CNNS nanocomposite. However, the reaction rate constants of CNNS, ZFNP, and ZFNP-CNNS are 0.0089, 0.0011, and 0.0452 min⁻¹, respectively, which shows that the ZFNP-CNNS nanocomposite dominates in the CIP removal with five times higher than pristine CNNS. Besides, the K_d and rate constant value of the ZFNP-CNNS nanocomposites exhibit a synergistic effect in the adsorption-photocatalytic processes. The adsorption of CIP molecules on the photocatalytic-adsorbent was also examined by various CIP concentrations ranging from 5 to 30 mg L⁻¹. Figure 3d presents that increasing CIP concentration increases the adsorption capacity until a saturation condition is reached. The contact time of

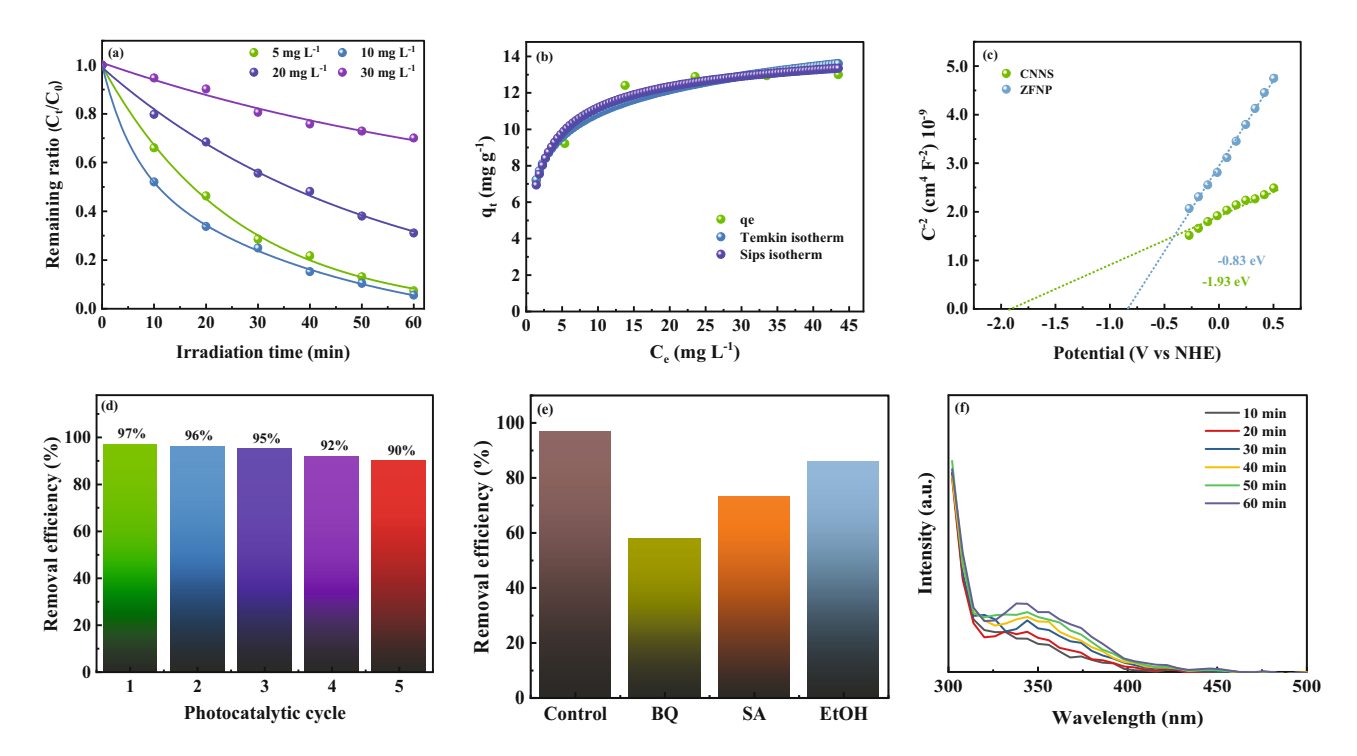


Figure 4: (a) The photocatalytic activity of the ZFNP-CNNS nanocomposite, (b) the exponential fitting of the Sips and Temkin isotherms, (c) Mott-Schottky plot, (d) the recyclability performance of the ZFNP-CNNS nanocomposite, and (e) the trapping experiment for reactive oxygen species (ROS), and (f) H_2O_2 production photodegradation of CIP.

 $30\,\mathrm{min}$ implies that the adsorption movement was adequate to achieve the adsorption equilibrium. The adsorption equilibrium is reached at 7.47, 9.06, 14.57, and 15.41 mg g⁻¹ for 5, 10, 20, and $30\,\mathrm{mg}\,\mathrm{L}^{-1}$ of CIP concentrations, respectively. To investigate the photocatalytic activity on CIP concentration-dependent activity, the CIP solution was exposed to a visible light for 60 min. The removal efficiency decreased by increasing the CIP concentration as depicted in Figure 4a. This result shows that high initial concentration of CIP can inhibit visible light to penetrate photocatalyst. Another reason is that the generation of by-products during the photodegradation reaction, which can compete with the initial CIP molecules, thus decreasing the surface contact between CIP molecules and photocatalyst material.

DE GRUYTER

Based on the theoretical and experimental data, the concentration-dependent adsorption capacity followed the good concurrent PSO kinetic models. PSO adsorption kinetics describes the involvement of multilayer in the adsorption process. Subject to the classification by Gile and Smith for the solute adsorption isotherm, the adsorption process of the ZFNP-CNNS nanocomposites is included in the L2-type isotherm [19]. This indicates that there is a high affinity between the adsorbate and the adsorbent as well as chemical bonds or electrostatic interactions in the multilayer adsorption process [31]. The Sips isotherm was used to investigate the nature of the adsorption process and examine the maximum adsorption capacity (Figure 4b). The Sips isotherm is the integration of the Langmuir and Freundlich model in heterogeneous systems. In addition, the Temkin model was also applied to assess the relationship between adsorption heat and binding. The Sips model represents an R^2 value of 0.961 with a maximum adsorption capacity of 15.49 mg g⁻¹, which approved that the CIP adsorption onto the ZFNP-CNNS nanocomposite follows the heterogeneous active sites with a multilayer adsorption process.

Meanwhile, the conduction band potentials ($E_{\rm CB}$) of CNNS and ZFNP are estimated to be -1.93 and -0.835 V (vs Ag/AgCl), which coincide with -1.33 and -0.23 V (vs NHE), respectively (Figure 4c). Moreover, the recyclability performance of the ZFNP–CNNS nanocomposites was also tested with five times recycling as depicted in Figure 4d. The removal efficiency of CIP was gradually reduced from the first cycle and reached 90% in the final cycle. The slight loss of photocatalytic performance indicates that the ZFNP–CNNS nanocomposite has excellent recyclability. Furthermore, according to the bandgap of 2.83 and 1.82 eV for CNNS and ZFNP, the calculated $E_{\rm VB}$ values are 1.50 and 1.59 V for CNNS and ZFNP, respectively. Based on the $E_{\rm g}$, $E_{\rm CB}$, and $E_{\rm VB}$ values, the proposed

reaction mechanism of the ZFNP-CNNS system is mentioned in the following equations.

$$ZFNP + hv \rightarrow ZFNP(e^- + h^+),$$
 (5)

$$e_{ZFNP}^- + CNNS \rightarrow ZFNP + e_{CNNS}^-,$$
 (6)

$$e_{(ZFNP-CNNS)}^- + O_2 \rightarrow O_2,$$
 (7)

$$0^{-}_{2} + e^{-} \rightarrow {}^{1}0_{2},$$
 (8)

$$0_{2}^{-} + Fe^{3+} \rightarrow {}^{1}O_{2} + Fe^{2+},$$
 (9)

$$2^{\circ}O_{2}^{-} + 2H^{+} \rightarrow O_{2} + H_{2}O_{2},$$
 (10)

$$Fe^{2+} + H_2O_2 \rightarrow Fe^{3+} + OH^- + OH,$$
 (11)

$$CIP + ZFNP - CNNS(h^+)/O_2/OH/O_2 \rightarrow CO_2 + H_2O.$$
 (12)

The trapping experiment was conducted to confirm the presence of ROS, which participated in the photodegradation of CIP. Hereinafter, several trapping agents were used, including 1,4-benzoquinone (BQ), sodium azide (SA), and ethanol (EtOH) as the scavengers to trap $^{1}O_{2}^{-}$, $^{1}O_{2}$, and $^{1}O_{1}$, respectively. Figure 4e shows the presence of BQ, SA, and EtOH in the photodegradation of CIP, which can reduce the photocatalytic performance of 58%, 73%, and 86%, respectively, indicating the presence of $^{1}O_{2}^{-}$, $^{1}O_{2}$, and $^{1}O_{1}$. Meanwhile, the generation of $^{1}O_{2}^{-}$ was determined using the spectrophotometry method. According to Figure 4f, the generation of $^{1}O_{2}^{-}$ increased in line with increasing reaction time. This result shows that the presence of $^{1}O_{2}^{-}$ also participates in the photodegradation of CIP.

Furthermore, the electrons could react with O_2 adsorbed on the surface of the photocatalytic adsorbent to produce O_2 . Then, the reduction process initiates with an appropriate potential reduction of $-0.33 \, \text{eV} \ (O_2/O_2) \ [32]$. The superoxide radical (O_2) is also capable of undergoing further reactions, producing other ROS family members. With a half-life of 2–4 ns, the superoxide radical (O_2) could be further transformed into more reactive species such as OH and O_2 . The presence of OH ions in ZFNP could facilitate the generation of OH in the valence band of CNNS could initiate the oxidation reaction of CIP directly because the energy level of the ZFNP–CNNS nanocomposite could not oxidize OH0 or OH1 to generate OH1 [33].

4 Conclusions

The ZFNP-CNNS nanocomposite was successfully synthesized with the simple calcination method. The ZFNP-CNNS nanocomposite exhibited an excellent adsorption-photocatalytic synergetic effect for CIP removal. Moreover, the

photodegradation efficiency of CIP reached up to five times compared to that of pristine CNNS. The adsorption isotherm study shows the heterogeneous active site with multilayer on the ZFNP–CNNS nanocomposite. The presence of an organic functional group and π – π interaction gives a sign that chemisorption participates in the ZFNP–CNNS system. On the other hand, the adsorption capacity of the ZFNP–CNNS nanocomposite is 15.49 mg g⁻¹. Finally, the experimental result presents that the ZFNP–CNNS nanocomposite is viable and has great application for wastewater treatment.

Funding information: This study was funded by the National Science and Technology Council (NSTC), Taiwan, for financial support under grant no. MOST 110-2221-E-007-058-MY3.

Author contributions: Muchammad Tamyiz: writing – original draft, writing – review and editing, visualization, methodology; and Ruey-an Doong: writing – review and editing, visualization, methodology, resources.

Conflict of interest: The authors state no conflict of interest.

Ethical approval: The conducted research is not related to either human or animal use.

Data availability statement: The datasets generated during and/or analyzed during the current study are available from the corresponding author on a reasonable request.

References

- [1] Sha J, Li L, An Z, He M, Yu H, Wang Y, et al. Diametrically opposite effect of Cu²⁺ on sulfamerazine and ciprofloxacin adsorption-photodegradation in g-C₃N₄/visible light system: behavior and mechanism study. Chem Eng J. 2022;428:131065. doi: 10.1016/j.cej.2021.131065.
- [2] Rafieenia R, Sulonen M, Mahmoud M, El-Gohary F, Rossa CA. Integration of microbial electrochemical systems and photocatalysis for sustainable treatment of organic recalcitrant wastewaters: Main mechanisms, recent advances, and present prospects. Sci Total Env. 2022;153923. doi: 10.1016/j. scitotenv.2022.153923.
- [3] Wang P, Tang Y, Dong Z, Chen Z, Lim T-T. Ag-AgBr/TiO₂/RGO nanocomposite for visible-light photocatalytic degradation of penicillin G. J Mater Chem A. 2013;1(15):4718-27. doi: 10.1039/C3TA01042B.
- [4] Zhang R, Jiang J, Zeng K. Synthesis of Bi₂WO₆/g-C₃N₄ heterojunction on activated carbon fiber membrane as a thin-film photocatalyst for treating antibiotic wastewater. Inorg Chem Commun. 2022;109418. doi: 10.1016/j.inoche.2022.109418.

- [5] Zhang J, Zheng Y, Zheng H, Jing T, Zhao Y, Tian J. Porous oxygen-doped g- C_3N_4 with the different precursors for excellent photocatalytic activities under visible light. Materials. 2022;15(4):1391. doi: 10.3390%2Fma15041391.
- [6] Adorna Jr J, Annadurai T, Bui TAN, Tran HL, Lin L-Y, Doong R-A. Indirect Z-scheme nitrogen-doped carbon dot decorated Bi₂MoO₆/g-C₃N₄ photocatalyst for enhanced visible-light-driven degradation of ciprofloxacin. Chem Eng J. 2021;422:130103. doi: 10.1016/j.cej.2021.130103.
- [7] Du R, Chen P, Zhang Q, Yu G. The degradation of enrofloxacin by a non-metallic heptazine-based OCN polymer: Kinetics, mechanism and effect of water constituents. Chemosphere. 2021;273:128435. doi: 10.1016/j.chemosphere.2020.128435.
- [8] Chen P, Di S, Qiu X, Zhu S. One-step synthesis of F-TiO₂/g-C₃N₄ heterojunction as highly efficient visible-light-active catalysts for tetrabromobisphenol A and sulfamethazine degradation. Appl Surf Sci. 2022;587:152889. doi: 10.1016/j.apsusc.2022.152889.
- [9] Lan Z-A, Zhang G, Wang X. A facile synthesis of Br-modified g-C₃N₄ semiconductors for photoredox water splitting. Appl Catal B. 2016;192:116-25. doi: 10.1016/j.apcatb.2016.03.062.
- [10] Mafa PJ, Malefane ME, Idris AO, Liu D, Gui J, Mamba BB, et al. Multi-elemental doped g-C₃N₄ with enhanced visible light photocatalytic Activity: Insight into naproxen degradation, kinetics, effect of electrolytes, and mechanism. Sep Purif Technol. 2022;282:120089. doi: 10.1016/j.seppur.2021. 120089.
- [11] Deng X, Wang D, Li H, Jiang W, Zhou T, Wen Y, et al. Boosting interfacial charge separation and photocatalytic activity of 2D/2D g-C₃N₄/ZnIn₂S₄ S-scheme heterojunction under visible light irradiation. J Alloy Compd. 2022;894:162209. doi: 10.1016/j.jallcom.2021.162209.
- [12] Zhang Y, Chen S, Meng Y, Chang L, Huang X, Zheng Y, et al. CNTs boosting superior cycling stability of ZnFe₂O₄/C nanoparticles as high-capacity anode materials of Li-ion batteries. J Alloy Compd. 2022;912:165135. doi: 10.1016/j.jallcom.2022. 165135.
- [13] Yang H, Hao H, Zhao Y, Hu Y, Min J, Zhang G, et al. An efficient construction method of S-scheme Ag₂CrO₄/ZnFe₂O₄ nanofibers heterojunction toward enhanced photocatalytic and antibacterial activity. Colloids Surf Physicochem Eng Asp. 2022;641:128603. doi: 10.1016/j.colsurfa.2022.128603.
- [14] Wu X, Lu J, Huang S, Shen X, Cui S, Chen X. Facile fabrication of novel magnetic 3-D ZnFe₂O₄/ZnO aerogel based heterojunction for photoreduction of Cr (VI) under visible light: controlled synthesis, facial change distribution, and DFT study. Appl Surf Sci. 2022;153486. doi: 10.1016/j.apsusc.2022.153486.
- [15] Luo J, Wu Y, Chen X, He T, Zeng Y, Wang G, et al. Synergistic adsorption-photocatalytic activity using Z-scheme based magnetic ZnFe₂O₄/CuWO₄ heterojunction for tetracycline removal. J Alloy Compd. 2022;910:164954. doi: 10.1016/j. jallcom.2022.164954.
- [16] Konicki W, Aleksandrzak M, Moszyński D, Mijowska E. Adsorption of anionic azo-dyes from aqueous solutions onto graphene oxide: Equilibrium, kinetic and thermodynamic studies. J Colloid Interface Sci. 2017;496:188–200. doi: 10.1016/j. jcis.2017.02.031.
- [17] Al-Ghouti MA, Da'ana DA. Guidelines for the use and interpretation of adsorption isotherm models: A review. J Hazard Mater. 2020;393:122383. doi: 10.1016/j.jhazmat.2020.122383.

- [18] Wang J, Guo X. Adsorption isotherm models: Classification, physical meaning, application and solving method. Chemosphere. 2020;258:127279. doi: 10.1016/j.chemosphere. 2020.127279.
- [19] Abbasi MA, Amin KM, Ali M, Ali Z, Atif M, Ensinger W, et al. Synergetic effect of adsorption-photocatalysis by GO -CeO2nanocomposites for photodegradation of doxorubicin. J Env Chem Eng. 2022;10(1):107078. doi: 10.1016/j.jece.2021.107078.
- [20] Wang S, Wang J. Magnetic 2D/2D oxygen doped g-C₃N₄/bio-char composite to activate peroxymonosulfate for degradation of emerging organic pollutants. J Hazard Mater. 2022;423:127207. doi: 10.1016/j.jhazmat.2021.127207.
- [21] Wu Y, Chen J, Che H, Gao X, Ao Y, Wang P. Boosting 2e oxygen reduction reaction in garland carbon nitride with carbon defects for high-efficient photocatalysis-self-Fenton degradation of 2, 4-dichlorophenol. Appl Catal B. 2022;307:121185. doi: 10.1016/j.apcatb.2022.121185.
- [22] Nguyen TB, Huang C, Doong R-A. Photocatalytic degradation of bisphenol A over a ZnFe₂O₄/TiO₂ nanocomposite under visible light. Sci Total Env. 2019;646:745–56. doi: 10.1016/j. scitotenv.2018.07.352.
- [23] Fan G, Lin X, You Y, Du B, Li X, Luo J. Magnetically separable ZnFe₂O₄/Ag₃PO₄/g-C₃N₄ photocatalyst for inactivation of Microcystis aeruginosa: Characterization, performance and mechanism. J Hazard Mater. 2022;421:126703. doi: 10.1016/j. jhazmat.2021.126703.
- [24] AL-Shwaiman HA, Akshhayya C, Syed A, Bahkali AH, Elgorban AM, Das A, et al. Fabrication of intimately coupled CeO₂/ZnFe₂O₄ nano-heterojunction for visible-light photocatalysis and bactericidal application. Mater Chem Phys. 2022;279:125759. doi: 10.1016/j.matchemphys.2022.125759.
- [25] Matli PR, Zhou X, Shiyu D, Huang Q. Fabrication, characterization, and magnetic behavior of porous ZnFe₂O₄ hollow microspheres. Nano Lett. 2015;5(1):53–9. doi: 10.1007/s40089-014-0135-2.
- [26] Nguyen TB, Doong R-A. Heterostructured ZnFe₂O₄/TiO₂ nanocomposites with a highly recyclable visible-light-response for

- bisphenol A degradation. RSC Adv. 2017;7(79):50006-16. doi: 10.1039/C7RA08271A.
- [27] Sarala E, Madhukara Naik M, Vinuth M, Rami Reddy Y, Sujatha H. Green synthesis of Lawsonia inermis-mediated zinc ferrite nanoparticles for magnetic studies and anticancer activity against breast cancer (MCF-7) cell lines. J Mater Sci Mater. 2020;31(11):8589–96. doi: 10.1007/s10854-020-03394-8.
- [28] Sarkar P, De S, Neogi S. Microwave assisted facile fabrication of dual Z-scheme g-C₃N₄/ZnFe₂O₄/Bi₂S₃ photocatalyst for peroxymonosulphate mediated degradation of 2, 4, 6-Trichlorophenol: the mechanistic insights. Appl Catal B. 2022;307:121165. doi: 10.1016/j.apcatb.2022.121165.
- [29] Shi Y, Li L, Xu Z, Sun H, Amin S, Guo F, et al. Engineering of 2D/3D architectures type II heterojunction with high-crystalline g-C₃N₄ nanosheets on yolk-shell ZnFe₂O₄ for enhanced photocatalytic tetracycline degradation. Mater Res Bull. 2022;111789. doi: 10.1016/j.materresbull.2022.111789.
- [30] Zheng X, Xu S, Wang Y, Sun X, Gao Y, Gao B. Enhanced degradation of ciprofloxacin by graphitized mesoporous carbon (GMC)-TiO2 nanocomposite: Strong synergy of adsorption-photocatalysis and antibiotics degradation mechanism. J Colloid Interface Sci. 2018;527:202–13. doi: 10.1016/j.jcis.2018.05.054.
- [31] Wang P, Wang X, Yu S, Zou Y, Wang J, Chen Z, et al. Silica coated Fe3O4 magnetic nanospheres for high removal of organic pollutants from wastewater. Chem Eng J. 2016;306:280–8. doi: 10.1016/j.cej.2016.07.068.
- [32] Sheng Y, Wei Z, Miao H, Yao W, Li H, Zhu Y. Enhanced organic pollutant photodegradation via adsorption/photocatalysis synergy using a 3D g-C₃N₄/TiO₂ free-separation photocatalyst. Chem Eng J. 2019;370:287–94. doi: 10.1016/j.cej.2019.03.197.
- [33] Saravanakumar K, Mamba G, Muthuraj V. 1D/2D MnWO₄ nanorods anchored on g-C₃N₄ nanosheets for enhanced photocatalytic degradation ofloxacin under visible light irradiation. Colloids Surf Physicochem Eng Asp. 2019;581:123845. doi: 10.1016/j.colsurfa.2019.123845.